J Mater Sci (2017) 52:1561–1572

Synthesis of MoO_3/WO_3 composite nanostructures for highly sensitive ethanol and acetone detection

Yongjiao Sun[1], Lin Chen[2], Ying Wang[1], Zhenting Zhao[1], Pengwei Li[1], Wendong Zhang[1], Yamin Leprince-Wang[3], and Jie Hu[1,*]

[1] *Micro and Nano System Research Center, Key Lab of Advanced Transducers and Intelligent Control System (Ministry of Education) & College of Information Engineering, Taiyuan University of Technology, No. 79 West Yingze Street, Taiyuan 030024, Shanxi, China*

[2] *Key Laboratory of Interface Science and Engineering in Advanced Materials (Taiyuan University of Technology), Ministry of Education, Taiyuan 030024, China*

[3] *Université Paris-Est, ESYCOM, UPEM, 5 bd. Descartes, 77454 Marne-la-Vallée, France*

Received: 7 July 2016
Accepted: 26 September 2016
Published online: 30 September 2016

ABSTRACT

In this paper, different contents of molybdenum oxide/tungsten oxide (MoO_3/WO_3) composite nanostructures were synthesized by hydrothermal method. Field emission scanning electron microscopy images revealed that the morphologies of WO_3 nanostructures were significantly influenced by the Mo amount. Furthermore, the introduction strategy of MoO_3 into WO_3 could effectively improve the gas sensing properties. Especially, the sensor based on the 4 mol% MoO_3/WO_3 composite nanostructures exhibited enhanced gas sensing performance, giving a low limit of detection (500 ppb). It shows high responses of 28.5 and 18.2–100 ppm ethanol and acetone at the operating temperature of 320 °C, which were about 2.3 and 1.7 times higher than those of the pure WO_3, respectively. The enhanced sensing properties of MoO_3/WO_3 gas sensor can be attributed to the addition of MoO_3, which has been discussed in relation to the gas sensing mechanism.

Introduction

Volatile organic compounds (VOCs; e.g., acetone, toluene, and formaldehyde) have high vapor pressure and fairly low boiling points, which make them evaporate easily at room temperature [1, 2]. VOCs have been recognized as the principal cause of many diseases including headaches, throat irritation, kidney disease, and even damage to the liver, lung, and the central nervous system [3–5]. Therefore, it is necessary to develop an efficient and convenient sensing technology for VOC detection [6, 7]. Compared with traditional gas sensing methods, semiconductor metal oxide gas sensors based on TiO_2, SnO_2, In_2O_3, WO_3, ZnO, Nb_2O_5, and MoO_3 have attracted great interest because of their high sensitivity, easy preparation, low consumption, and high integrability properties [8–12].

Address correspondence to E-mail: hujie@tyut.edu.cn

DOI 10.1007/s10853-016-0450-2

Among these metal oxide semiconductor materials, WO_3 is considered to be the most promising material due to its remarkable performance and practical application in gas detection [13, 14]. Recently, great efforts have been made to further improve the gas sensing performance of WO_3 gas sensor using various methods such as improving the specific surface area [15], decreasing the grain size [16], doping with noble metal [17], and forming the heterojunction [18]. For example, Chi et al. synthesized WO_3 nanotubes using electrospinning technique, and the as-prepared WO_3 gas sensor showed low limit of detection (2.5–0.5 ppm) and quick response/recovery time (5/22 s) to acetone [19]. Yang et al. fabricated Au-functionalized WO_3 gas sensor under mild conditions, and the measured response could reach 63.6 for 10 ppm *n*-butanol, which is about 60 times higher than that of the pure one [20]. Zhao et al. prepared Co_3O_4–WO_3 heterojunction gas sensor for acetone detection, and the response was about two times that of pure WO_3 sensor [21]. According to the previous works, it has been demonstrated that introducing extrinsic dopants is one of the most facile and effective ways to improve the gas sensing performance of WO_3 gas sensor toward the target gases. However, to the best of our knowledge, few studies have been focused on MoO_3/WO_3 composite nanostructures for ethanol and acetone detection.

Herein, the pure WO_3 and different MoO_3/WO_3 composite nanostructures have been successfully synthesized by a one-step hydrothermal method. The obtained results show that the morphology and gas sensing performance of MoO_3/WO_3 nanostructures are critically dependent on the Mo content. Especially, the 4 mol% MoO_3/WO_3 gas sensor exhibits the highest response, low limit of detection, excellent selectivity, and good stability. Meanwhile, to further understand the enhanced gas sensing performance, the mechanisms of the MoO_3/WO_3 composite were also studied.

Experimental

Chemicals

Tungsten hexachloride ($WCl_6 \geq 99.9$ %) and ammonium heptamolybdate tetrahydrate ($(NH_4)_6Mo_7O_{24}{\cdot}4H_2O \geq 99.0$ %) were purchased from Sigma-Aldrich. Absolute ethanol was obtained from Sinopharm Chemical Reagent Company. All reagents were of analytical grade and were used as received without further purification.

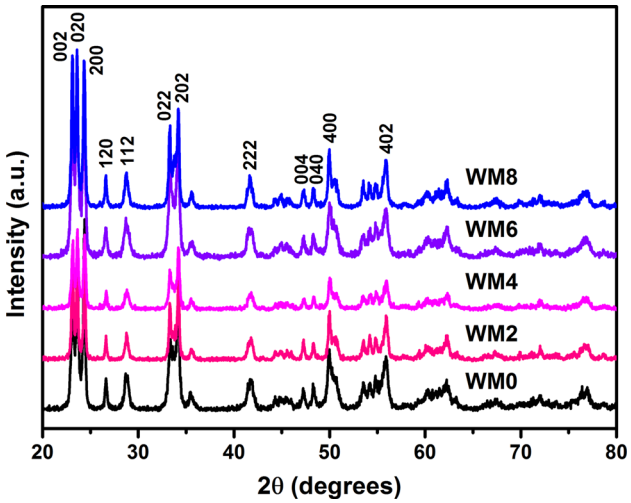

Figure 1 XRD patterns of the pure WO_3 and MoO_3/WO_3 composite nanostructures.

Sample preparation

In a typical process, 1.51 mmol of WCl_6 and a definite amount (0, 2, 4, 6, and 8 mol %) of $(NH_4)_6Mo_7O_{24}{\cdot}4H_2O$ were added into 60 mL of absolute ethanol. After stirring vigorously for 30 min, the homogeneous solution was transferred into a Teflon-lined stainless steel autoclave and heated at 160 °C for 24 h. After cooling to room temperature naturally, the precipitate was collected and dried at 80 °C for 10 h. Finally, the as-prepared product was calcined at 500 °C for 2 h. For convenience, pure WO_3 and MoO_3/WO_3 samples were labeled as WM0 and WM*x* ($x = 2$, 4, 6, and 8), which corresponds to the mole ratios of Mo and W.

Characterization

X-ray powder diffraction (XRD) analysis was performed using a DRIGC-Y 2000A X-ray diffractometer with Cu-Kα_1 radiation ($\lambda = 1.5406$ Å) and the scanning speed was 6° min^{-1}. Field emission scanning electron microscope (FESEM) images were recorded on a JEOL JSM-7001F microscope operating at 15 kV which is equipped with a QUANTAX 200 energy-dispersive spectrometer (EDS) for elemental analyses. X-ray photoelectron spectroscopy (XPS) analysis was carried out using an ESCALAB 250Xi. The specific surface areas and the cumulative volume of pores of the sample were determined using Tristar 3020

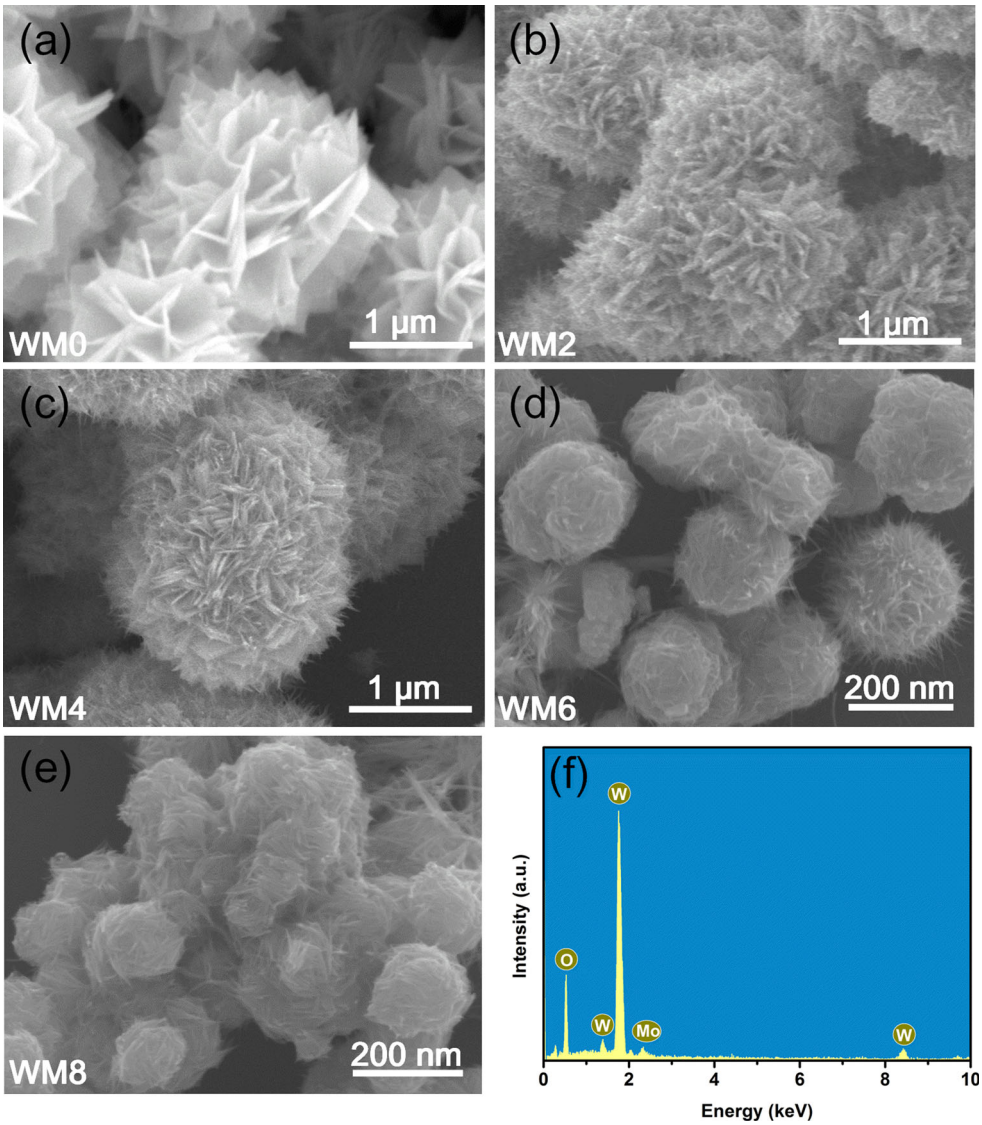

Figure 2 SEM images of **a** WM0, **b** WM2, **c** WM4, **d** WM6, and **e** WM8 and **f** EDS spectrum of sample WM8.

Brunauer–Emmett–Teller (BET) and Barrett–Joyner–Halenda (BJH) methods.

Gas sensing measurements

The fabrication process of gas sensor can be described as follows: firstly, the as-calcined sample was mixed with deionized water to form a paste and coated on a ceramic tube (4 mm in length, 1.2 mm in external diameter, and 0.8 mm in internal diameter) attached with a pair of Au electrodes and Pt wires. After that, the element was sintered at 500 °C for 2 h after drying in the shade. Then, a Ni–Cr alloy coil heating wire was inserted into the tube as a heater to keep the sensor working at a given temperature. The measurements of the gas sensing properties were carried out using static test method with CGS-4TP intelligent analysis system (Elite, Beijing, China). The relative humidity in the measurement atmosphere was maintained at about 30 %. We denote by R_a and R_g the resistances in air and in the target gas, respectively. Then the response (R) of the gas sensor to the target gas was defined as the ratio of R_a to R_g. The response and recovery times were defined as the time for 90 % of the total resistance change and the time for 90 % recovery of the resistance change, respectively.

Results and discussion

Structure analysis

The crystal structures of the pure WO_3 and MoO_3/WO_3 composite were investigated using XRD.

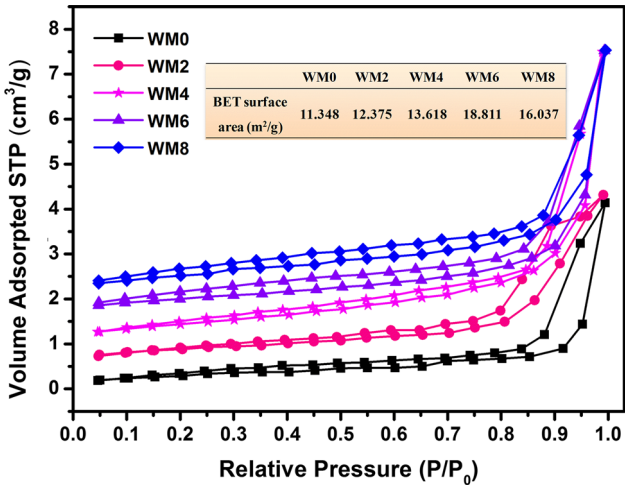

Figure 3 Nitrogen adsorption–desorption isotherms of pure WO_3 and MoO_3/WO_3 composite nanostructures. *Inset* table shows the corresponding BET surface areas.

Figure 1 shows the XRD patterns of the as-obtained samples after annealing at 500 °C. Distinct characteristic peaks ((002), (020), and (200)) were clearly observed. The main diffraction peaks of all samples correspond to the monoclinic phase [space group $P2_1/n(14)$] of WO_3 with the lattice parameters $a = 7.297$ Å, $b = 7.539$ Å, $c = 7.688$ Å, and $\beta = 90.91°$, which is well consistent with the standard JCPDS card No. 43-1035. Moreover, no diffraction peak shifts or obvious diffraction peak of MoO_x was observed, which is probably due to the relatively low amount of Mo in the samples. However, when the content of Mo in WO_3 was increased to 20 mol%, the diffraction peaks of MoO_3 were obtained (Supporting Information Fig. S1).

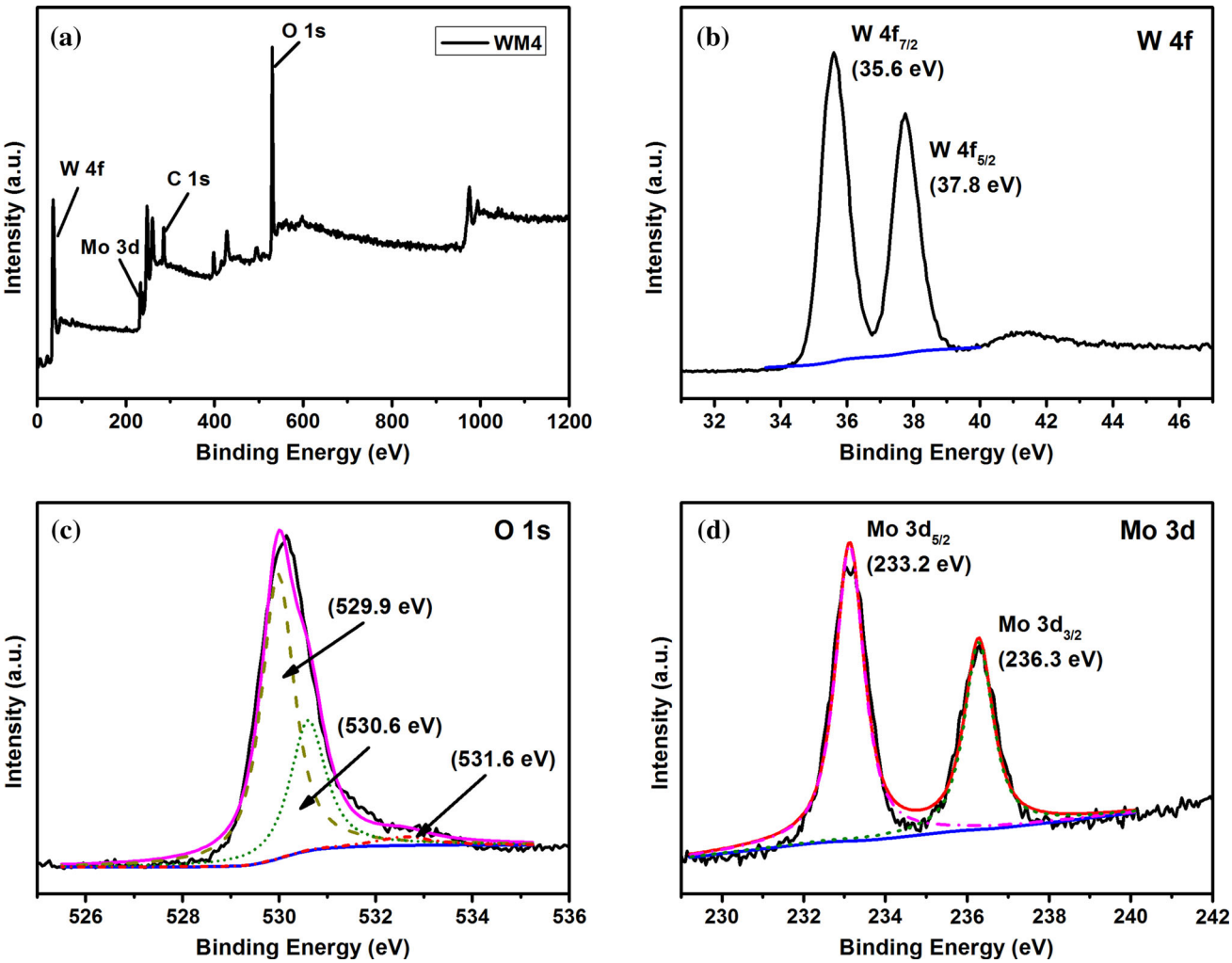

Figure 4 **a** XPS survey spectrum of WM4. High-resolution XPS scan of **b** W 4*f* region, **c** O 1*s* region, and **d** Mo 3*d* region.

Morphological analysis

The morphologies of the as-prepared WO_3 samples were observed using FESEM. Figure 2a presents the pure WO_3 sample, exhibiting a flower-like structure with diameters ranging from 1.5 to 2 μm and composed of intersecting nanoflakes. For MoO_3/WO_3 samples, it seems that the introduction of Mo element can significantly influence the morphology. Figure 2b, c shows the MoO_3/WO_3 samples WM2 and WM4, which were composed of two-tier structures with lots of fluffs on the surface. With further increasing the content of Mo, the nanoflake structures were replaced by nanoparticles (Fig. 2d, e), and the sizes of the samples decrease from 230 to 180 nm. The measured results show that the presence and the content of Mo element have significant influence on the morphology of MoO_3/WO_3 composite nanostructures. Similar results have been reported in many previous works regarding this phenomenon [22, 23]. To confirm the existence of Mo, EDS was conducted on sample WM8 as shown in Fig. 2f. The peaks correspond to W, O, and Mo elements. No other impurity element was observed, indicating the high purity of the samples. Meanwhile, the elemental mapping experiment was also conducted on WM8, which further confirms the uniform distribution of Mo (Fig. S2 in Supporting Information).

The BET surface areas and porous structures were investigated by nitrogen adsorption–desorption using BET and BJH methods. Figure 3 shows the nitrogen adsorption–desorption isotherms of all the as-prepared samples. According to the IUPAC classification, it can be found that both pure WO_3 and MoO_3/WO_3 nanostructures have isotherms of type II with a type H3 hysteresis loop, which implies nonporous structures. The inset table shows the corresponding BET surface areas of the pure WO_3 and MoO_3/WO_3 composite nanostructures. It can be clearly observed that the surface area of the as-prepared samples increased at the initial stage, reached the maximum value for WM6 (18.811 m^2/g), and decreased with a further increase in the concentration of Mo. The larger surface area of sensing materials normally results in more active sites on the surface for chemical or physical interactions, thereby giving rise to better sensing performance [24].

XPS results

To further determine the elemental compositions and chemical oxidation valance state, XPS measurements

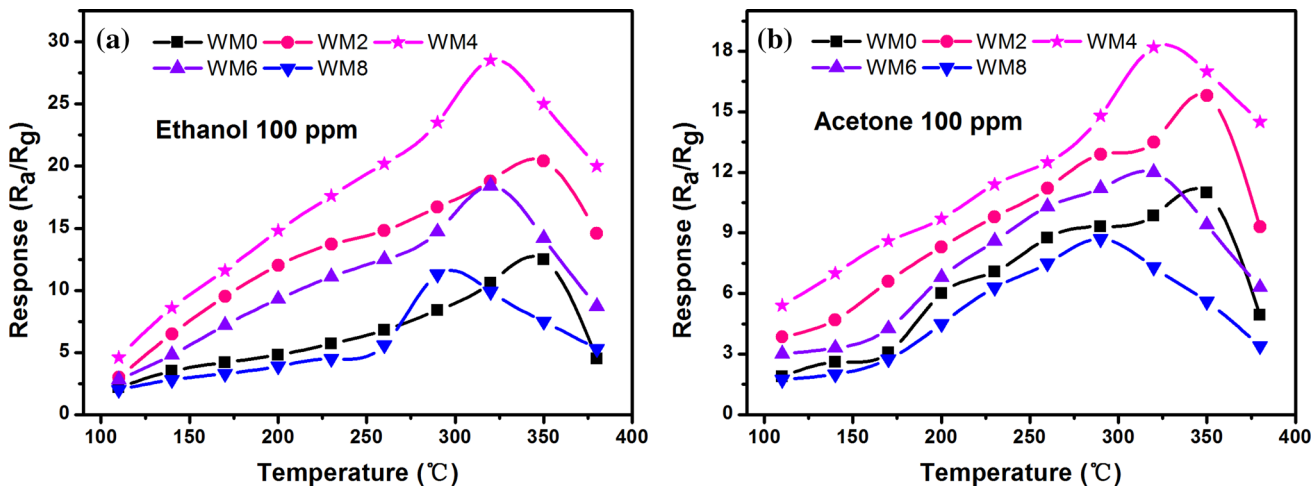

Figure 5 Responses of pure WO_3 and MoO_3/WO_3 nanostructures to 100 ppm **a** ethanol and **b** acetone as a function of temperature.

Table 1 The optimum operating temperatures of all samples toward ethanol and acetone

Sample	WM0 °C	WM2 °C	WM4 °C	WM6 °C	WM8 °C
Ethanol	350	350	320	320	290
Acetone	350	350	320	320	290

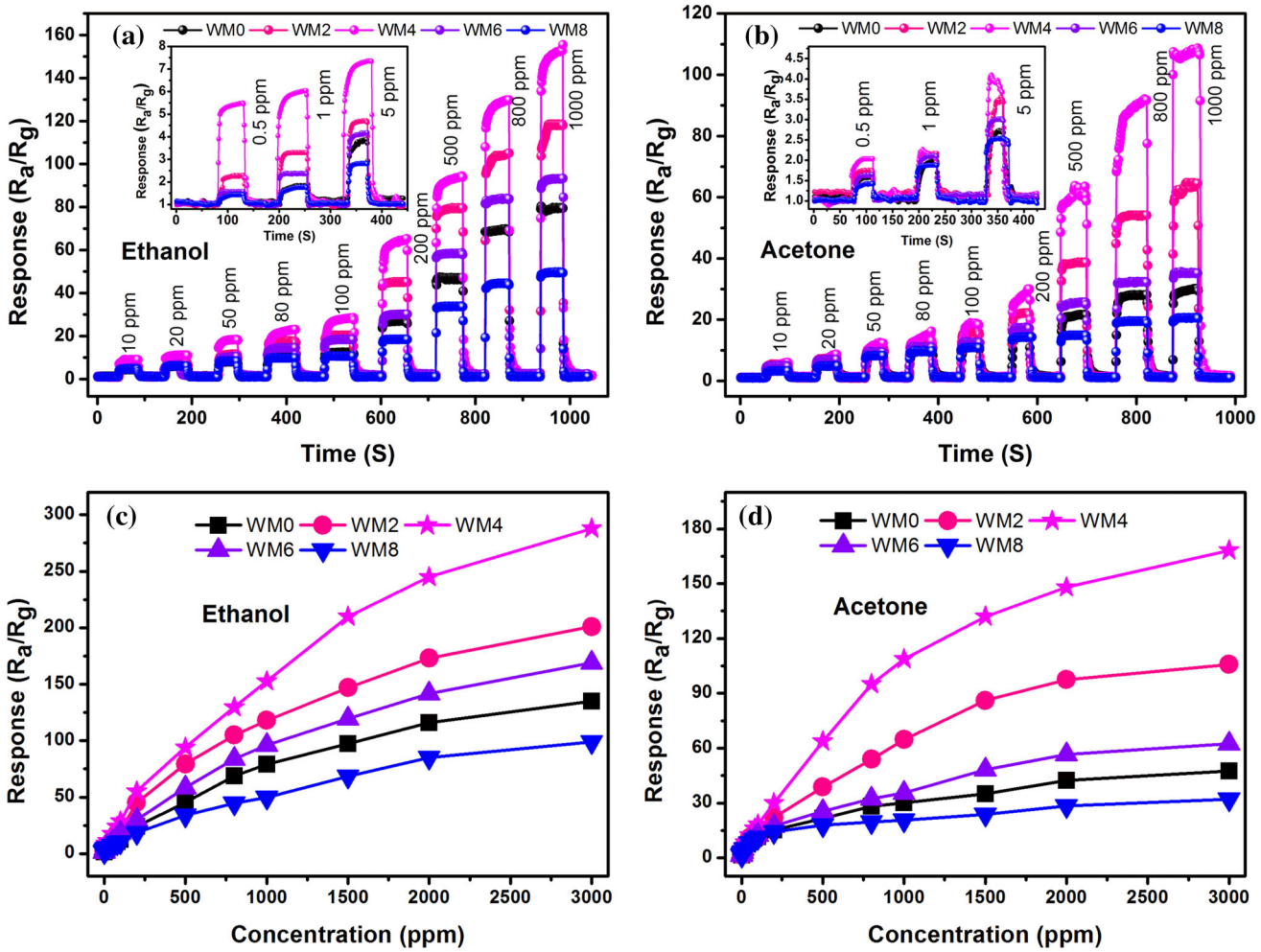

Figure 6 Dynamic sensing characteristics of the as-prepared gas sensors to different concentrations of **a** ethanol and **b** acetone at their optimum operating temperatures; response versus concentration curves of all the samples toward **c** ethanol and **d** acetone.

were conducted on WM4. The binding energies were calibrated by referencing the C 1*s* peak (284.6 eV) to reduce the sample charging effect. Figure 4a exhibits the XPS survey spectrum of WM4 with a binding energy ranging from 0 to 1200 eV, and the main constituent elements were tungsten, molybdenum, and oxygen. Figure 4b shows the high-resolution scan of W 4*f*. The doublets of W $4f_{7/2}$ and W $4f_{5/2}$ peaks, located at 35.6 and 37.8 eV, correspond to W–O bond, which is well consistent with previous works [25–27]. Figure 4c illustrates the high-resolution spectrum of O 1*s*, which can be fitted into three symmetrical Gaussian peaks. The corresponding peaks located at 529.9 and 530.6 eV can be ascribed to lattice oxygen in WO_3. The third peak at 531.6 eV might be due to the chemically adsorbed oxygen [16]. Figure 4d displays the Mo 3*d* spectrum, which can be deconvoluted into two major peaks with binding energies at 233.2 and 236.3 eV, corresponding to Mo $3d_{5/2}$ and Mo $3d_{3/2}$, respectively. The measured results indicate that Mo element exists mainly in the Mo^{6+} chemical state in MoO_3, which is in accordance with the results of XRD [28].

Gas sensing characteristics

It is well known that the working temperature plays an important role in the gas sensing performance of a gas sensor [20, 29]. To investigate the gas sensing property, the temperature dependence behavior of all the as-fabricated gas sensors to 100 ppm ethanol and acetone was evaluated under different temperatures, as shown in Fig. 5a, b. The results reveal that the responses of all sensors increased with the operating temperature and achieved their maximum values. Further increase in the operating temperature results

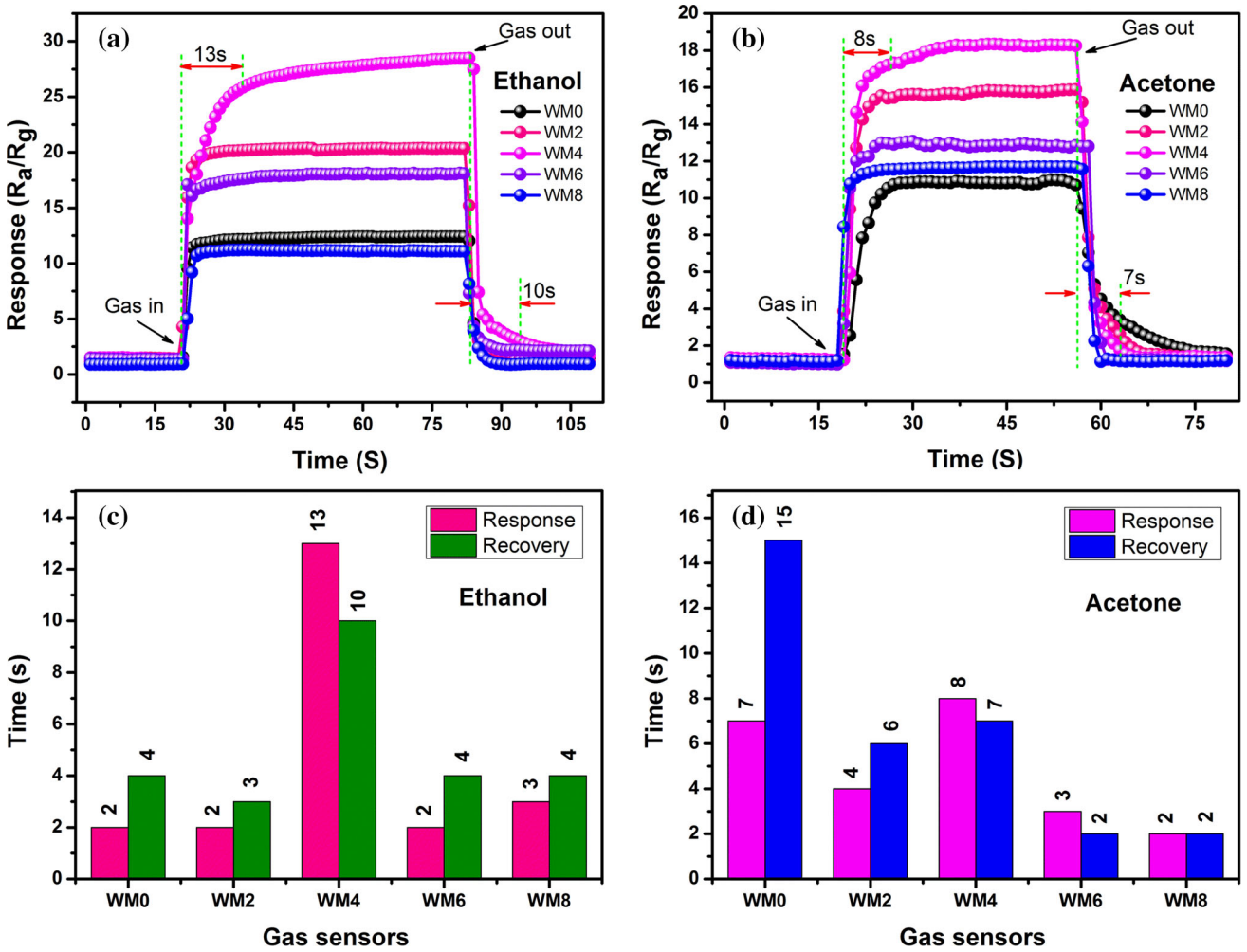

Figure 7 Response transients of the as-fabricated sensors exposed to 100 ppm **a** ethanol and **b** acetone at their optimum operating temperatures and the response and recovery times of all sensors toward **c** ethanol and **d** acetone.

in the decrease of responses. Moreover, the measured results show that the WM4 exhibits the maximum response values of 28.5 and 18.2 toward 100 ppm ethanol and acetone at 320 °C, respectively, which is much higher than that of pure WO_3 sensor (12.5 and 10.9 for ethanol and acetone). Consequently, an optimum working temperature of 320 °C was chosen for the remainder of the experiments on WM4 gas sensor. Table 1 presents the detailed information on the optimum operating temperatures for all the as-prepared gas sensors, and it seems that the optimum operating temperature decreases with the increase of the Mo amount.

Figure 6a, b shows the dynamic sensing transients of the pure WO_3 and MoO_3/WO_3 composite nanostructures to 0.5–1000 ppm of ethanol and acetone under optimum operating temperatures. When the gas sensors were exposed to target gases, the response of all the as-prepared gas sensors shows a clear increase with the increase of gas concentration. The results reveal that the gas sensors based on WM2, WM4, and WM6 exhibit higher sensibility at each concentration than WM0. In particular, the WM4 sensor exhibits the highest responses for target gases, and the sensitivities are about 2.3 and 1.7 times higher than those of WM0 sensor for 100 ppm ethanol and acetone, respectively, while the WM8 sensor even displays slightly lower response than WM0, which indicates that the excessive MoO_3 may suppress the gas sensing properties of sensor. Furthermore, when the ethanol/acetone concentration is as low as 500 ppb, the measured sensitivities of WM4 sensor could still reach 5/2.3, which demonstrates that the sensor could detect the concentrations of

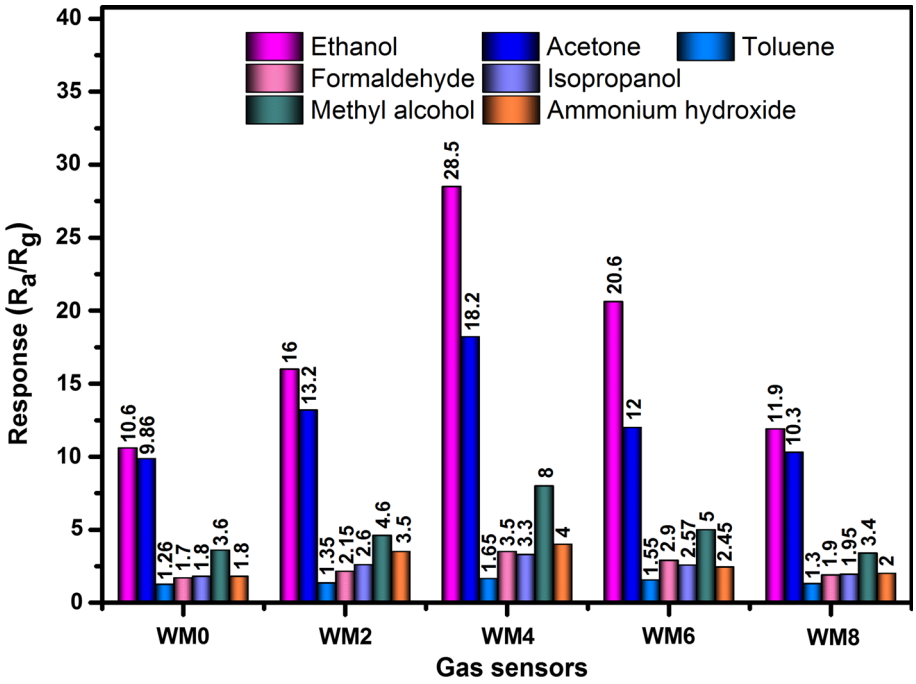

Figure 8 Selectivity of pure and MoO_3/WO_3 gas sensors to different VOCs at a concentration of 100 ppm at their optimum operating temperatures.

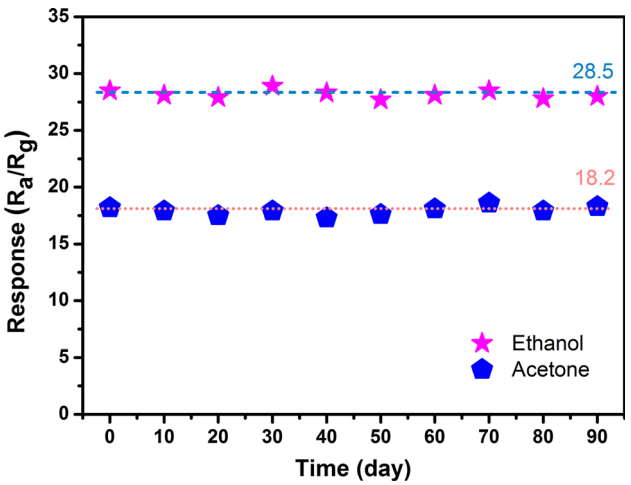

Figure 9 Long-term stability of the gas sensor based on WM4 toward 100 ppm ethanol and acetone.

ethanol and acetone down to ppb level. Therefore, the WM4 gas sensor is potentially used in monitoring trace ethanol and acetone.

Figure 6c, d illustrates the response versus concentration curves of all samples toward ethanol and acetone. The measured results show that all the as-prepared gas sensors show a rapidly increasing response with increasing target gas concentration (0.5–3000 ppm). Especially, the WM4 sensor shows the best gas sensing performance to ethanol and acetone under different concentrations. The responses of WM4 sensor to 1000 ppm ethanol (152.7) and acetone (108.7) are remarkably higher than those of WM0 (95 and 40.2), indicating the enhanced gas sensing properties. However, the gas response values begin to plateau as the concentration of target gas increases further, which suggests that the sensors gradually tend to saturate. The saturation effect can be explained by the competition between the adsorption sites and the concentration of the target gas [30]. The surface reaction is linearly dependent on the tested gas concentration as long as the adsorption sites are enough. In the low gas concentration of ethanol and acetone, the available adsorption sites on the surface of WM*x* can be regarded as infinite, and the rate-determining step might be the surface reaction between target gas molecules and WM*x* surface. However, at a high concentration of target gas, the gas molecules have to compete for adsorption sites due to the insufficiency of available adsorption sites on the surface of WM*x*, which becomes the rate-determining step.

Figure 7a, b shows the response/recovery curves of all the as-fabricated gas sensors to 100 ppm ethanol and acetone at their optimum operating temperatures. The gas sensors' responses reached the certain values or returned to the initial values quickly when they were exposed to or released from the target gases. Figure 7c shows the response/recovery times of as-fabricated gas sensors to ethanol, and most of

Table 2 Gas sensing properties of various WO_3 nanostructures to ethanol and acetone reported in the literatures and the present study (WM4 sensor)

Sensing materials	Gas type	Concentration (ppm)	T(°C)	R	T_{res}/t_{rec} (s)	LOD (ppm)	Ref.
Flower-like WO_3 architectures	Ethanol	100	300	7	1/6	–	[13]
	Acetone	100	300	4	2/9		
Co_3O_4-modified WO_3 NRs	Acetone	100	280	5.30	–/–	6	[21]
	Ethanol	100	280	<4.5	–/–	–	
Co-doped WO_3 nanofibers	Acetone	20	300	4.89	–/–	0.25	[34]
	Ethanol	20	300	2.31	–/–	–	
WO_3–Cr_2O_3 thin films	Acetone	20	320	8.91	–/–	0.5	[35]
	Ethanol	20	320	<2	–/–	–	
WO_3 nanobricks	Ethanol	100	300	6.5	3/5	20	[36]
Ag-sensitized WO_3 hollow nanospheres	Ethanol	500	230	73.4	>30/>20	1	[37]
WO_3 nanocuboids	Ethanol	100	300	3.55	–/–	–	[38]
Au/WO_3	Ethanol	20000	300	178	–/–	–	[39]
WO_3 thin films	Ethanol	185	150	10.2	180/288	12	[40]
WM4	Ethanol	100	320	28.5	13/10	0.5	This work
	Acetone	100		18.2	8/7	0.5	

T Temperature, *R* response, t_{res}response time, t_{rec} recovery time, *LOD* limit of detection

gas sensors exhibit quick response/recovery behaviors within 3/4 s. Figure 7d displays the response/recovery times of sensors to acetone, the corresponding response/recovery times are within 3/4 s except the pure WO_3 sensor. The relatively fast response and recovery times compared to bulk WO_3 can be associated to the special hierarchical structures. The hierarchical structures composed of nanosheets/nanowires would form network pores, grain boundaries, and junction barriers, which are beneficial for the gas diffusion, oxygen diffusion, and re-adsorption [31–33].

Selectivity is another important parameter of gas sensors for their practical application. The selectivity was also investigated on pure WO_3 and MoO_3/WO_3 gas sensors. Figure 8 illustrates the bar graph of the as-prepared sensors to 100 ppm of variety of VOCs, such as ethanol, acetone, methyl alcohol, formaldehyde, ammonium hydroxide, and toluene. All gas sensors exhibit higher responses to ethanol than the other gases, which suggest that the as-fabricated gas sensors exhibit outstanding selectivity to ethanol. At the same time, the long-term stability experiments were conducted on WM4 gas sensor every 10 days for 3 months (Fig. 9). The measured results show that the responses of WM4 sensor toward ethanol and acetone are fluctuating slightly around 28.5 and 18.2, respectively, which confirms the excellent long-term stability of WM4 composite nanostructures. In addition, a comparison between the sensing performances of WM4 sensor and literature reports is summarized in Table 2. It is noteworthy that the WM4 sensor exhibits higher response compared with other nanostructured WO_3 sensors reported in previous works.

Gas sensing mechanism

For pure WO_3, when the gas sensor was exposed to air, the thickness of electron depletion layer will increase due to the ionization of oxygen molecules. Therefore, the resistance of WO_3 will increase, which result from the lower concentration of free electrons in the conduction band (Fig. 10a). When the gas sensor was exposed to reducing gases, the oxygen species will react with the target gas and release electrons into the conduction band. Thus, the thickness of the depletion layer at the interfaces will decrease, which will lead to the decrease of the measured resistance of the WO_3 gas sensor (Fig. 10b).

Compared with pure WO_3, the enhanced gas sensing properties of MoO_3/WO_3 gas sensor can be attributed to the synergetic effect and the heterojunction of WO_3 and MoO_3. Firstly, both MoO_3 and WO_3 are important sensing materials. There is a synergetic effect of different gas sensing materials, which has been observed in the other hierarchical composites [41–43]. Secondly, it can be ascribed to the

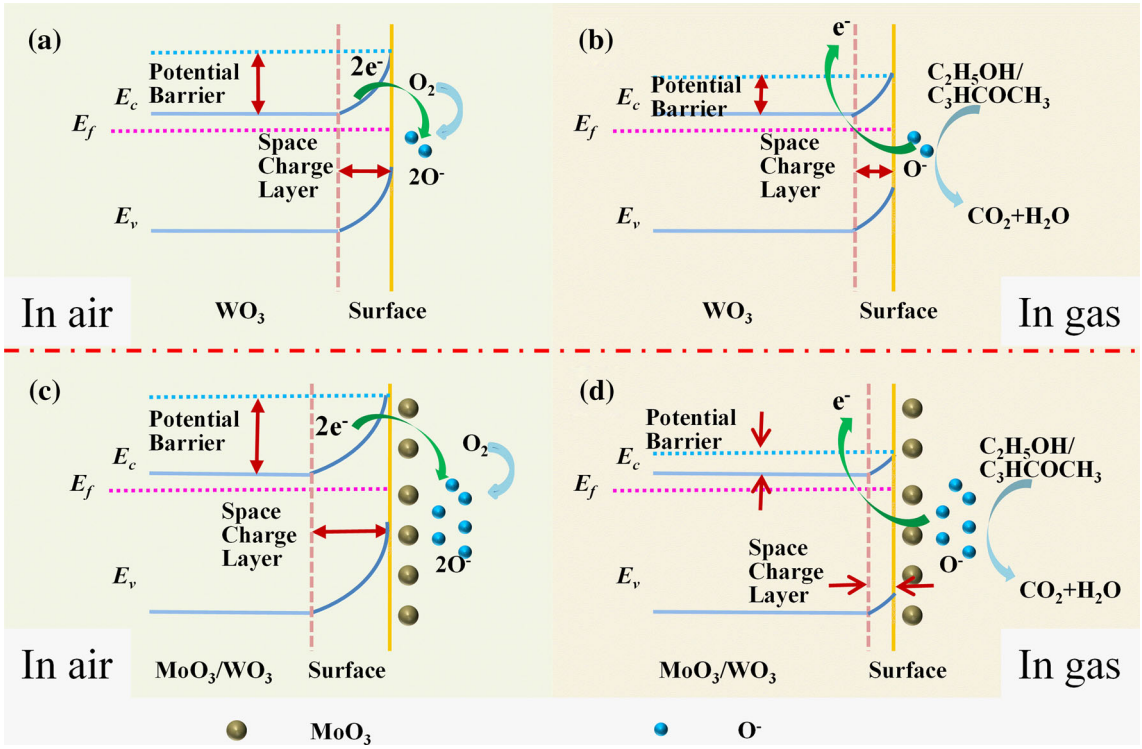

Figure 10 Schematic band diagrams of pure WO_3 and MoO_3/WO_3 exposed to air and target gas.

heterojunction, which formed at the interface between MoO_3 and WO_3. The different work functions will lead to the negatively charged carries moving from WO_3 to MoO_3 until their Fermi levels align, creating a thicker electron depletion layer at the interface (Fig. 10c, d) [20, 44]. As a result, it exhibits enhanced sensing property to ethanol and acetone than pure WO_3. The sensing mechanism controlled by the change of the electron depletion layer thickness has also been found in other composites [45, 46]. However, the excessive content of Mo element will suppress the sensing properties of the samples, because excess dopant would reduce the available adsorption sites between WO_3 and the target gas, which is in agreement with the previous report [47].

Conclusions

In summary, pure WO_3 and MoO_3/WO_3 composite nanostructures were successfully synthesized and characterized. The SEM results show that the morphology of WO_3 can be greatly affected by the content of Mo. The gas sensing properties were measured on pure WO_3 and MoO_3/WO_3 gas sensors and the results suggest that the moderate introduction of MoO_3 could significantly improve the gas sensing properties. Moreover, the WM4 gas sensor exhibits enhanced responses to ethanol and acetone, which are about 2.3 and 1.7 times higher than those of pure WO_3 gas sensor, respectively. The low limit of detection of WM4 can be down to 500 ppb. The enhanced gas sensing performance of the MoO_3/WO_3 may be attributed to the synergetic effects of MoO_3 and WO_3. This study will be beneficial for the construction of WO_3-based composite gas sensors with higher response, fast response/recovery time, and good selectivity and stability for trace ethanol and acetone detection.

Acknowledgements

We appreciate the support of the National Natural Science Foundation of China (51205274), Shanxi Province Science Foundation (2016011039), Shanxi Province Special Talent Fund (201605D211020), University of Science and Technology innovation Research Project of Shanxi Province (2016137), Graduate Education Innovation Fund (02100738), Science and Technology Major Project of the Shan Xi Science and Technology Department (20121101004),

and Key Disciplines Construction in Colleges and Universities of Shanxi [(2012)45].

Electronic supplementary material: The online version of this article (doi:10.1007/s10853-016-0450-2) contains supplementary material, which is available to authorized users.

References

[1] Kim YS, Ha SC, Yang H, Kim YT (2007) Gas sensor measurement system capable of sampling volatile organic compounds (VOCs) in wide concentration range. Sens Actuator B 122:211–218

[2] Dar GN, Umar A, Zaidi SA, Ibrahim AA, Abaker M, Baskoutas S (2012) Ce-doped ZnO nanorods for the detection of hazardous chemical. Sens Actuators B 173:72–78

[3] Rakshit T, Santra S, Manna I, Ray SK (2014) Enhanced sensitivity and selectivity of brush-like SnO_2 nanowire/ZnO nanorod heterostructure based sensors for volatile organic compounds. RSC Adv 4:36749–36756

[4] Rai P, Majhi SM, Yu Y-T, Lee J-H (2015) Synthesis of plasmonic Ag@SnO_2 core–shell nanoreactors for xylene detection. RSC Adv 5:17653–17659

[5] Jia QQ, Ji HM, Zhang Y, Chen YL, Sun XH, Jin ZF (2014) Rapid and selective detection of acetone using hierarchical ZnO gas sensor for hazardous odor markers application. J Hazard Mater 276:262–270

[6] Shin J, Choi SJ, Youn DY, Kim D (2012) Exhaled VOCs sensing properties of WO_3 nanofibers functionalized by Pt and IrO_2 nanoparticles for diagnosis of diabetes and halitosis. J Electroceram 29:106–116

[7] Zeng Y, Zhang T, Wang LJ, Kang MH, Fan HT, Wang R, He Y (2009) Enhanced toluene sensing characteristics of TiO_2-doped flowerlike ZnO nanostructures. Sens Actuators B 140:73–78

[8] Rani RA, Zoolfakar AS, Ou JZ, Field MR, Austin M, Kalantar-zhadeh K (2013) Nanoporous Nb_2O_5 hydrogen gas sensor. Sens Actuators B 176:149–156

[9] Mao YZ, Ma S, Li XB, Wang CY, Li FM (2014) Effect of Mn doping on the microstructures and sensing properties of ZnO nanofibers. Appl Surf Sci 298:109–115

[10] Dong CJ, Xing XX, Chen N, Liu X, Wang YD (2016) Biomorphic synthesis of hollow CuO fibers for low-ppm-level *n*-propanol detection via a facile solution combustion method. Sens Actuators B 230:1–8

[11] Sun P, Wang C, Liu JY, Zhou X, Li XW, Hu XL, Lu GY (2015) Hierarchical assembly of α-Fe_2O_3 nanosheets on SnO_2 hollow nanospheres with enhanced ethanol sensing properties. ACS Appl Mater Interfaces 7:19119–19125

[12] Vuong NM, Hieu NM, Kim D, Choi B, Kim M (2014) Ni_2O_3 decoration of In_2O_3 nanostructures for catalytically enhanced methane sensing. Appl Surf Sci 317:765–770

[13] Wang ZY, Sun P, Yang TL, Gao Y, Li XW, Lu GY, Du Y (2013) Flower-like WO_3 architectures synthesized via a microwave-assisted method and their gas sensing properties. Sens Actuator B 186:734–740

[14] Wang C, Sun R, Li X, Sun YF, Sun P, Liu FM, Lu GY (2014) Hierarchical flower-like WO_3 nanostructures and their gas sensing properties. Sens Actuator B 204:224–230

[15] Zeng J, Hu M, Wang WD, Chen HQ, Qin YX (2012) NO_2-sensing properties of porous WO_3 gas sensor based on anodized sputtered tungsten thin film. Sens Actuator B 161:447–452

[16] Zhang YD, He WW, Zhao HX, Li PJ (2013) Template-free to fabricate highly sensitive and selective acetone gas sensor based on WO_3 microspheres. Vacuum 95:30–34

[17] Xu LJ, Yin ML, Liu SZ (2015) Superior sensor performance from Ag@WO_3 core–shell nanostructure. J Alloys Compd 623:127–131

[18] Kida T, Nishiyama A, Hua ZQ, Suematsu K, Yuasa M (2014) WO_3 nanolamella gas sensor: porosity control using SnO_2 nanoparticles for enhanced NO_2 sensing. Langmuir 30:2571–2579

[19] Chi X, Liu CB, Li Y, Wang ZJ, Bo XQ, Liu LL, Su C (2014) Tungsten trioxide nanotubes with high sensitive and selective properties to acetone. Sens Actuator B 194:33–37

[20] Yang XJ, Salles V, Kaneti Y, Liu MS, Maillard M, Journet C, Jiang XC, Brioude A (2015) Fabrication of highly sensitive gas sensor based on Au functionalized WO_3 composite nanofibers by electrospinning. Sens Actuator B 220:1112–1119

[21] Zhao XD, Ji HM, Jia QQ, Wang MJ (2015) A nanoscale Co_3O_4–WO_3 p–n junction sensor with enhanced acetone responsivity. J Mater Sci 26:8217–8223. doi:10.1007/s10854-015-3484-3

[22] Wang CY, Ma SY, Sun A, Qin R, Yang FC, Li XB (2014) Characterization of electrospun Pr-doped ZnO nanostructure for acetic acid sensor. Sens Actuator B 193:326–333

[23] Sun P, Zhou X, Wang C, Wang B, Xu XM, Lu GY (2014) One-step synthesis and gas sensing properties of hierarchical Cd-doped SnO_2 nanostructures. Sens Actuators B 190:32–39

[24] Lu YY, Zhan WW, He Y, Wang YT, Kong XJ, Kuang Q, Xie ZX, Zheng LS (2014) MOF-templated synthesis of porous Co_3O_4 concave nanocubes with high specific surface area and their gas sensing properties. ACS Appl Mater Interface 6:4186–4195

[25] Zhou D, Shi F, Xie D, Wang DH, Xia XH, Wang XL, Gu CD, Tu JP (2016) Bi-functional Mo-doped WO_3 nanowire array electrochromism-plus electrochemical energy storage. J Colloid Interface Sci 465:112–120

[26] Zhou D, Xie D, Shi F, Wang DH, Ge X, Xia XH, Wang XL, Gu CD, Tu JP (2015) Crystalline/amorphous tungsten oxide core/shell hierarchical structures and their synergistic effect for optical modulation. J Colloid Interface Sci 460:200–208

[27] Cai GF, Tu JP, Zhou D, Wang XL, Gu CD (2014) Growth of vertically aligned hierarchical WO_3 nano-architecture arrays on transparent conducting substrates with outstanding electrochromic performance. Sol Energy Mater Sol Cells 124:103–110

[28] Swiatowska-Mrowiecka J, de Diesbach S, Maurice V, Zanna S, Klein L, Briand E, Vickridge I, Marcus P (2008) Li-ion intercalation in thermal oxide thin films of MoO_3 as studied by XPS, RBS, and NRA. J Phys Chem C 112:11050–11058

[29] Kaneti YV, Zakaria QMD, Zhang Z, Chen C, Yue J, Liu M, Jiang XC, Yu A (2014) Solvothermal synthesis of ZnO-decorated α-Fe_2O_3 nanorods with highly enhanced gas-sensing performance toward *n*-butanol. J Mater Chem A 2:13283–13292

[30] Ahn MW, Park KS, Heo JH, Kim DW, Choi KJ, Park JG (2009) On-chip fabrication of ZnO-nanowire gas sensor with high gas sensitivity. Sens Actuator B 138:168–173

[31] Huang JR, Xu XJ, Gu CP, Yang M, Yang M, Liu JH (2011) Large-scale synthesis of hydrated tungsten oxide 3D architectures by a simple chemical solution route and their gas-sensing properties. J Mater Chem 21:12283–13289

[32] Sun P, Wang WN, Liu YP, Sun YF, Ma J, Lu GY (2012) Hydrothermal synthesis of 3D urchin-like α-Fe_2O_3 nanostructure for gas sensor. Sens Actuator B 173:52–57

[33] Alenezi MR, Henley SJ, Emerson NG, Silva RP (2014) From 1D and 2D ZnO nanostructures to 3D hierarchical structures with enhanced gas sensing properties. Nanoscale 6:235–247

[34] Jia QQ, Ji HM, Gao P, Bai X, Jin ZG (2015) Control of the acetone sensitive and selective properties of WO_3 nanofibers by doping Co ions: effect of crystal symmetric structure on the responsivity of gas–solid boundaries for gas sensor. J Mater Sci 26:5792–5802. doi:10.1007/s10854-015-3138-5

[35] Gao P, Ji HM, Zhou YG, Li XL (2012) Selective acetone gas sensors using porous WO_3–Cr_2O_3 thin films prepared by sol–gel method. Thin Solid Film 520:3100–3106

[36] Xiao JK, Song CW, Dong W, Li C, Yin YY, Zhang XN, Song MY (2015) Synthesis, characterization, and gas sensing applications of WO_3 nanobricks. J Mater Eng Perform 24:3026–3031

[37] Yao Y, Ji FX, Yin ML, Ren XP, Ma Q, Yan JQ (2016) Ag nanoparticle-sensitized WO_3 hollow nanosphere for localized surface plasmon enhanced gas sensors. ACS Appl Mater Interface 8:18165–18172

[38] Li XX, Zhang GY, Cheng FY, Guo B, Chen J (2006) Synthesis, characterization, and gas-sensor application of WO_3 nanocuboids. J Electrochem Soc 153:H133–H137

[39] Labidi A, Gillet E, Delamare R, Maaref M, Aguir K (2006) Ethanol and ozone sensing characteristics of WO_3 based sensors activated by Au and Pd. Sens Actuator B 120: 338–345

[40] Ahsan M, Ahmad MZ, Tesfamichael T, Bell J, Wlodarski W, Motta N (2012) Low temperature response of nanostructured tungsten oxide thin films toward hydrogen and ethanol. Sens Actuator B 173:789–796

[41] Chen YJ, Zhu CL, Shi XL, Cao MS, Jin HB (2008) The synthesis and selective gas sensing characteristics of SnO_2/α-Fe_2O_3 hierarchical nanostructures. Nanotechnology 19:205603

[42] Zhu CL, Chen YJ, Wang RX, Wang LJ, Cao MS, Shi XL (2009) Synthesis and enhanced ethanol sensing properties of α-Fe_2O_3/ZnO heteronanostructures. Sens Actuator B 140:185–189

[43] Sun P, Cai YX, Du SS, Xu XM, You L, Ma J, Liu FM, Liang XS, Sun YF, Lu GY (2013) Hierarchical α-Fe_2O_3/SnO_2 semiconductor composites: hydrothermal synthesis and gas sensing properties. Sens Actuator B 182:336–343

[44] Majhi Bertouluzzi L, Tietwyk KJ, Ginsburg A, Keller DA, Yaro PL, Anderson AY, Bisquert J, Zaban A (2016) Combinatorial investigation and modelling of MoO_3 hole-selective contact in TiO_2/Co_3O/MoO_3 all-oxide solar cells. Adv Mater Interface 3:1–7

[45] Lundstrom KI, Shivaraman MS, Syensson CM (1975) A hydrogen-sensitive Pd-gate MOS transistor. J Appl Phys 46:3876–3881

[46] Yu J, Wlodarski W, Li YX, Kalantar-zadeh K (2010) Nanorod based Schottky contact gas sensors in reversed bias condition. Nanotechnology 21:265502

[47] Liu CB, Shan H, Liu L, Li SC, Li HY (2014) High sensing properties of Ce-doped α-Fe_2O_3 nanotubes to acetone. Ceram Int 40:2395–2399